nature physics

Article

https://doi.org/10.1038/s41567-023-02060-0

Dirac revivals drive a resonance response in twisted bilayer graphene

Received: 12 August 2022

Accepted: 18 April 2023

Published online: 11 May 2023

Check for updates

Erin Morissette[1], Jiang-Xiazi Lin[1], Dihao Sun[1], Liangji Zhang[2], Song Liu[3], Daniel Rhodes[3], Kenji Watanabe[4], Takashi Taniguchi[5], James Hone[3], Johannes Pollanen[2], Mathias S. Scheurer[6], Michael Lilly[7], Andrew Mounce[7] ✉ & J. I. A. Li[1] ✉

Collective excitations contain key information regarding the electronic order of the ground state of strongly correlated systems. Various collective modes in the spin and valley isospin channels of magic-angle graphene moiré bands have been alluded to by a series of recent experiments. However, a direct observation of collective excitations has been impossible due to the lack of a spin probe. Here we observe low-energy collective excitations in twisted bilayer graphene near the magic angle, using a resistively detected electron spin resonance technique. Two independent observations show that the generation and detection of microwave resonance relies on the strong correlations within the flat moiré energy band. First, the onset of the resonance response coincides with the spontaneous flavour polarization at moiré half-filling, but is absent in the isospin unpolarized density range. Second, we perform the same measurement on various systems that do not have flat bands and observe no indication of a resonance response in these samples. Our explanation is that the resonance response near the magic angle originates from Dirac revivals and the resulting isospin order.

Within the flat energy band of magic-angle graphene moiré systems, the influence of the Coulomb interaction gives rise to prominent instabilities, which are commonly described by spontaneous polarization in the internal flavour degrees of freedom of the moiré unit cell, given by spin, valley and flatband degeneracy[1–3]. This process results in a reconstructed band structure with well-defined isospin order. As most emergent quantum phases, such as correlated insulators[4–6], superconductivity[4,6,7] and topological ferromagnetism[8–13], are associated with different forms of flavour polarization, studying the process of flavour polarization and the resulting isospin order is essential to understand the nature of electronic order in graphene moiré systems. Conventionally, experimental efforts rely on the evolution of the energy gap with the in-plane magnetic field to determine the underlying isospin configuration. Given the requirement of a robust energy gap and well-defined thermal activation behaviour, this method is only applicable to insulating states. Moreover, there is a multitude of possible isospin configurations. In the case of the simultaneous presence or close competition of different isospin orders, which is often the case in magic-angle graphene moiré systems, the magnetic-field (B) dependence of the gap might not be enough to reveal the ground-state order. This lack of viable experimental methods contributes to a sizable gap in our understanding of the moiré flatband. For instance, intervalley Hund's interaction J_H describes the coupling of electron spins across opposite valleys. The value and sign of J_H are crucial for a wide variety

[1]Department of Physics, Brown University, Providence, RI, USA. [2]Department of Physics and Astronomy, Michigan State University, East Lansing, MI, USA. [3]Department of Mechanical Engineering, Columbia University, New York, NY, USA. [4]Research Center for Functional Materials, National Institute for Materials Science, Tsukuba, Japan. [5]International Center for Materials Nanoarchitectonics, National Institute for Materials Science, Tsukuba, Japan. [6]Institute for Theoretical Physics, University of Innsbruck, Innsbruck, Austria. [7]Center for Integrated Nanotechnologies, Sandia National Laboratories, Albuquerque, NM, USA. ✉e-mail: amounce@sandia.gov; jia_li@brown.edu

https://doi.org/10.1038/s41567-023-02060-0

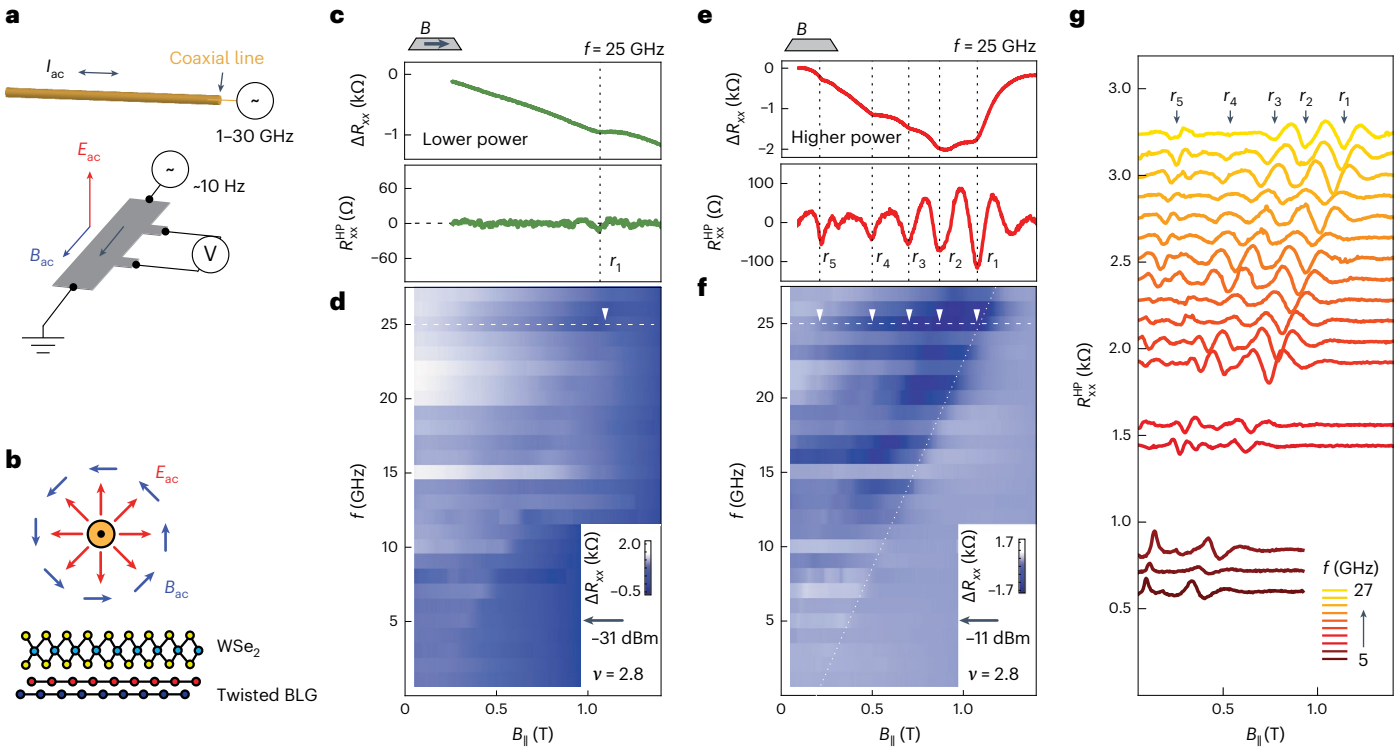

Fig. 1 | Microwave-induced transport response in TBG. a, Schematic of the device measurement setup, including the microwave coaxial line I_{ac} proximally above the Hall bar channel. Microwave signal with frequency within 1–30 GHz passes through the coaxial line. Longitudinal resistance R_{xx} is measured from the sample with a small current bias of ~5 nA at a near-d.c. frequency of 17 Hz. **b**, According to the geometry of the setup, the magnetic (electric) component of the microwave field, B_{ac} (E_{ac}), is aligned parallel (perpendicular) to the graphene sheets. **c**–**f**, Influence of microwave radiation on the transport response of the sample measured at $\nu = 2.8$. ΔR_{xx} is the change in longitudinal resistance compared with $B = 0$. R_{xx}^{HP} is obtained by applying an HPF to eliminate the slow-varying background in ΔR_{xx}. ΔR_{xx} and R_{xx}^{HP} measured with low microwave power of 0.8 dBm (**c** and **d**) and high microwave power of 16.8 dBm (**e** and **f**). ΔR_{xx} (**c** and **e**, top) and R_{xx}^{HP} (**c** and **e**, bottom) as a function of an in-plane magnetic field $B_{\parallel}$. In **d** and **f**, ΔR_{xx} is a function of an in-plane magnetic field $B_{\parallel}$ and microwave frequency f. **g**, Waterfall plot of R_{xx}^{HP} as a function of $B_{\parallel}$ measured at different microwave frequencies. Locations of r_1–r_5 are marked with vertical arrows.

of theoretical studies of superconductivity and correlated insulators in magic-angle graphene moiré systems[14–24]. However, even the sign of J_H has remained unknown to date, owing to the scarcity of experimental constraints and the fact that the contributions of Coulomb and electron–phonon interactions are of similar magnitude but of opposite sign[18].

The ability to examine collective excitations could establish a new route to identify electronic orders within a moiré flatband, as the nature of these collective excitations is determined by the isospin order of the underlying ground state[21,22,24–26]. The existence of these collective modes has been hinted at by the observation of large electronic entropy within the moiré flatband[27–29]. It is argued that the tendency to flavour polarize gives rise to fluctuating local flavour moments at a high temperature, which contributes to the large residual entropy and the associated Pomeranchuk-like transition. Furthermore, collective isospin fluctuations might also provide the pairing glue or at least crucially influence the form and strength of superconductivity. This highlights the importance of studying collective excitations to better understand the nature of electronic orders in the moiré flatband.

In this work, we report the observation of collective excitations near magic-angle twisted bilayer graphene (TBG) using the resistively detected electron spin resonance technique. Collective excitations are generated when the energy of microwave photons matches the energy of the collective mode. If the generation of excitation gives rise to a change in the sample resistivity, it is detectable using standard d.c. transport techniques (see the 'Transport measurement' section in the Supplementary Information for more details). The observation of electron spin resonance establishes the first direct experimental identification of collective excitations in TBG, which allows us to identify the nature of spin coupling across opposite valleys and extract parameters that characterize the spin properties.

The setup for the resonance measurement is illustrated in Fig. 1a,b. A coaxial line is placed above and perpendicular to the TBG sample shaped into a Hall bar geometry. As a microwave signal is applied to the coaxial line between 1 and 28 GHz with source powers between −120 and 21 dBm, it irradiates the device with microwave photons. Figure 1c–g shows the transport response across a TBG sample in the presence of an in-plane magnetic field with varying power and frequency levels in the microwave radiation at moiré filling $\nu = 2.8$, which falls within the density range of $2 < |\nu| < 3$. Microwave radiation induces prominent changes in the longitudinal resistance of the sample, ΔR_{xx}. At low microwave power ($P = -31$ dBm) and $f = 5$ GHz, ΔR_{xx} exhibits a single dip (Fig. 1c, vertical dashed line). The location of this dip follows a linear trajectory in the f–B map (Fig. 1d). At higher microwave power, the dip in ΔR_{xx} becomes more pronounced (Fig. 1e, top). At the same time, this transport response widens to occupy a larger area in the f–B map (Fig. 1f). The fact that increasing the microwave power produces more prominent changes in the sample resistance suggests that these features originate from the coupling between microwave photons and electrons in the moiré flatband. The application of a high-pass filter (HPF) eliminates the slow-varying background in ΔR_{xx} as a function of an in-plane magnetic field, which yields R_{xx}^{HP}. Although R_{xx}^{HP} exhibits a similar behaviour as ΔR_{xx} at low microwave power, it reveals five separate features at high power, which are manifested as sharp minima in R_{xx}^{HP}. The location of these features are marked by the vertical dashed lines and white arrows in Fig. 1c–g. For simplicity, we will refer to these

https://doi.org/10.1038/s41567-023-02060-0

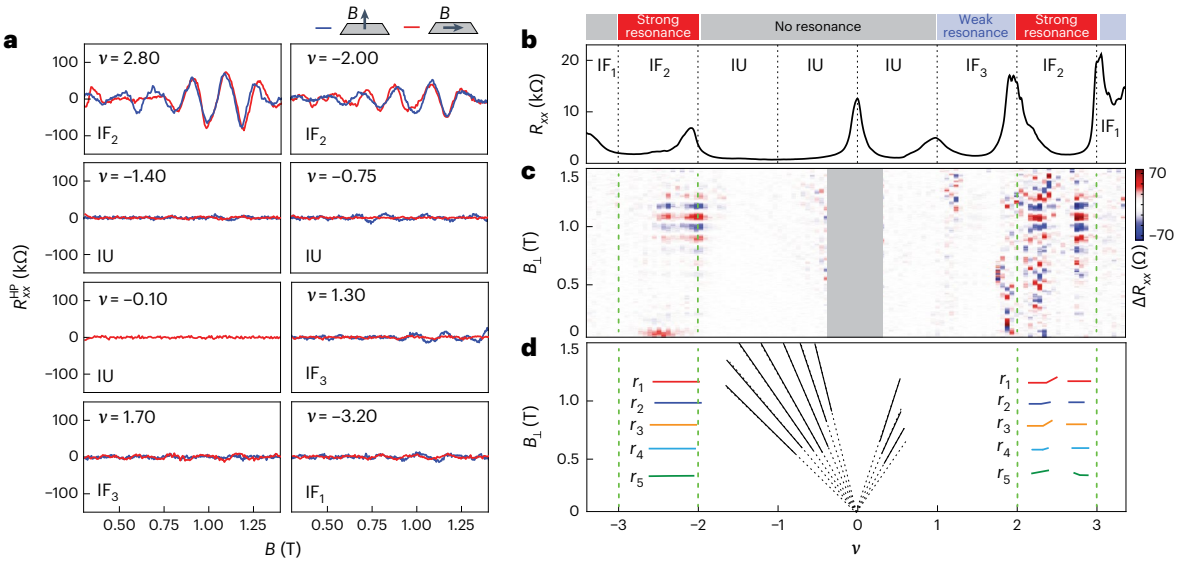

Fig. 2 | Density dependence and magnetic anisotropy. a, R_{xx}^{HP} as a function of $B_\perp$ and $B_\parallel$, measured at a range of different moiré fillings in the presence of microwave radiation with $f = 27$ GHz. The sample is highly resistive at the CNP ($\nu = -0.1$) in the presence of an out-of-plane B field. Therefore, only the dependence on $B_\parallel$ is plotted. The slight oscillation in the $B_\perp$ dependence at $\nu = -1.40$ and -0.75 derives from quantum oscillation emanating from the CNP (Supplementary Fig. 18c). **b**, R_{xx} as a function of filling measured at $T = 20$ mK and $B = 10$ mT. Resistance peaks in R_{xx} separate symmetry-breaking isospin ferromagnets (IF_2 and IF_3) and IU states. The density range of the observed microwave-induced resonance is marked on the top axis. **c**, R_{xx}^{HP} as a function of filling fraction ν and $B_\perp$ measured at microwave frequency $f = 27$ GHz. **d**, Location of resonance modes r_1–r_5 marked in a schematic of the ν–B map. The solid coloured lines denote the locations of the resonance modes. The boundaries of IF_2 are marked with the green vertical dashed lines in **c** and **d**. The black lines mark the location of quantum Hall effect states observed near the CNP.

features as resonance modes r_1–r_5. Figure 1g shows the waterfall plot of R_{xx}^{HP} versus an in-plane magnetic field $B_\parallel$ measured at different microwave frequencies f. The positions of r_1–r_5 are identified as sharp minima. The evolution of r_1–r_5 with varying f and B values follows well-defined linear trajectories across a wide frequency range, namely, $5 < f < 30$ GHz.

Two observations testify that r_1 is the fundamental resonance mode. First, the dependence of these resonances on varying microwave powers shows that r_1 emerges at the lowest microwave power over all the frequencies (Supplementary Fig. 1). Second, the microwave power dependence shows that the resonance mode with a lower excitation energy, defined by its location in the f–B map at a lower frequency, is more robust compared with one with higher energy, with r_1 (r_4) being the most (least) robust (Fig. 1c–e). One of the main focuses of this work is to understand the origin of r_1. We will also examine the condition required for detecting electron spin resonance using resistive methods in encapsulated graphene samples. Furthermore, we offer experimental characterization and theoretical interpretation for all the other resonance modes.

The energy of the microwave photon provides an important clue regarding the origin of the observed resonance modes. A 10 GHz microwave photon corresponds to an energy of 0.04 meV. The observation of the resonance response indicates that electrons must be able to absorb microwave photons and transition into an excited state, producing a change in sample resistivity at the same time. Owing to the strong Coulomb correlation in a moiré flatband, the energy gap associated with flavour polarization and Fermi surface reconstruction is on the order of several millielectronvolts[5,6,30]. As a result, particle–hole excitations across these correlation-driven gaps require an energy that far exceeds the photon energy. As such, the excited states corresponding to r_1–r_5 must be associated with low-energy collective excitations that are below the continuum of interband particle–hole excitations. As an in-plane magnetic field is mostly decoupled from valley and sublattice degrees of freedom[31], the collective excitation must emerge from the spin channel.

Figure 2 plots the dependence of the resonance response on moiré filling, which reveals a direct link between the flat moiré band and the observed resonance behaviour[1,2,27]. Figure 2a plots R_{xx}^{HP} at $f = 27$ GHz as a function of both in-plane and out-of-plane magnetic fields, namely, $B_\parallel$ and $B_\perp$, respectively, measured at different moiré fillings. Prominent resonance response is observed near half-filling of both electron- and hole-doped moiré bands, at $\nu = 2.8$ and -2.0, respectively. At these moiré fillings, the resonance signal remains the same for both out-of-plane and in-plane magnetic fields, which is consistent with excitations from the spin channel (Supplementary Fig. 3). In particular, the presence of a strong spin–orbit coupling leads to resonance behaviours that generically depend on the B-field orientation. The fact that the resonance frequencies are unaltered when the magnetic field is rotated in and out of the plane of the system indicates that the influence of the spin–orbit coupling is not crucial for the spectrum of excitations, giving rise to microwave resonance features (Fig. 2a and Supplementary Fig. 3). We note, however, that despite the weak impact of the spin–orbit coupling onto the spectrum of these modes, symmetry reduction due to the nearby WSe_2 layer could be crucial for an efficient coupling of microwaves and the collective modes, as well as their impact on the transport.

Most interestingly, the transport measurement shows no resonance response near the charge neutrality point (CNP). In this regime, a slight variation in R_{xx}^{HP} develops with an increasing out-of-plane magnetic field, which corresponds to quantum oscillations emanating from the CNP. Similarly, the resonance response is absent, or extremely weak, around one-quarter and three-quarter fillings. To gain more insights into the density dependence of resonance behaviour, Fig. 2b,c compares the resonance response, shown as horizontal features with blue and red colours (Fig. 2c), with the dependence of longitudinal resistance R_{xx} on moiré filling ν across the moiré flatband. As shown in Fig. 2b, the emergence of resistance peaks near integer moiré fillings of $\nu = -2$, $+1$ and $+2$ is in excellent agreement with previous experiments on magic-angle TBG[1,2,12,27,28]. These resistance peaks, along with resets

https://doi.org/10.1038/s41567-023-02060-0

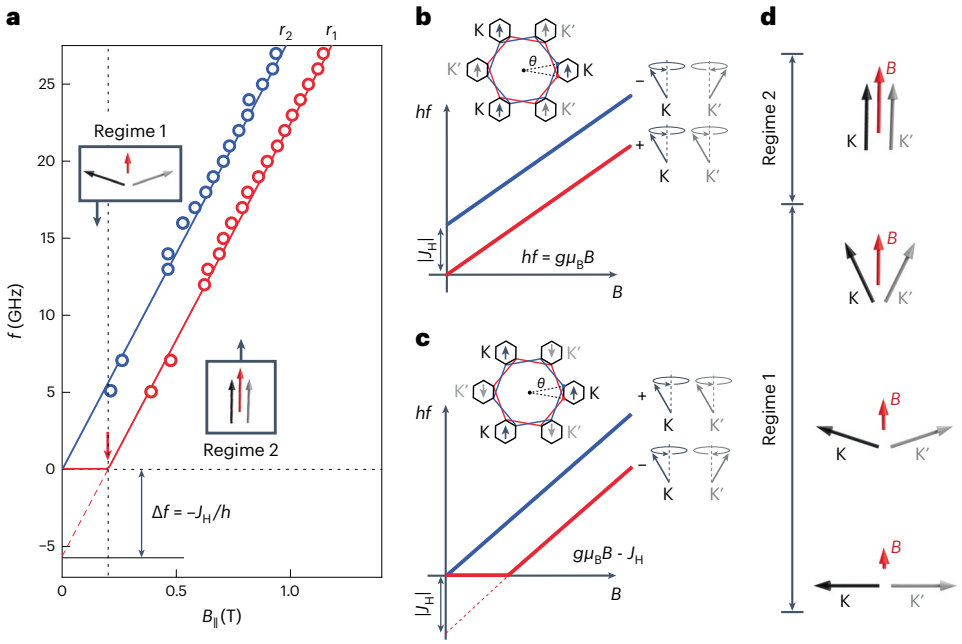

Fig. 3 | Antiferromagnetic intervalley coupling and the value of J_H. a, Locations of r_1 and r_2 in the f–B trajectories, fit by a spin magnon model where the primary mode extrapolates to a negative intercept $\Delta f = -J_H/h$, with intervalley Hund's coupling J_H. **b**,**c**, Schematic of energy hf versus B trajectories for ferromagnetic coupling ($J_H < 0$) in which the spins are aligned in the two valleys (and along the external magnetic field) (**b**) and antiferromagnetic coupling ($J_H > 0$) (**c**). **d**, Anti-parallel spins develop an increasingly large ferromagnetic component along the field (regime 1) and perfectly align with it in the two valleys above a critical field (regime 2). The insets in **b** and **c** depict the schematic of the moiré Brillouin zone, showing the nature of intervalley spin order.

in Hall density (Supplementary Fig. 16), define the boundaries of different isospin orders resulting from Dirac revival. The isospin order of the underlying Fermi surface away from integer filling can be identified based on the main sequence of quantum oscillations (Supplementary Figs. 17 and 19). Based on these characterizations, we label different regimes of the moiré band fillings according to the underlying isospin order, such as isospin unpolarized (IU) and isospin ferromagnet with N-fold degeneracy, IF_N (Fig. 2c). Here N takes the values of 1, 2 and 3, which corresponds to the degeneracy in quantum oscillation. Strong resonance responses (Fig. 2c) show excellent agreement with the density range of IF_2 on both electron- and hole-doping side of the moiré band. The robust resonance near half-filling, contrasting with the lack of a resonance response near the CNP, places an important constraint on the possible origin of the resonance response. A natural explanation is that these are collective excitations associated with textures in the flavour degrees of freedom, such as the magnon modes (Fig. 3c).

In the density range identified as IF_3 or IF_1, a microwave-induced resonance response is mostly absent, despite the presence of 'Dirac revival'. The lack of resonance in these regimes may be the result of a few different factors. First, the magnitude of the resonance behaviour could depend on the strength of isospin flavour polarization. In magic-angle TBG, half-filling at $\nu \pm 2$ often hosts the most prominent correlation-driven states with the most robust energy gap, whereas the energy gaps at one-quarter and three-quarter fillings are only partially developed. Second, the different isospin orders of IF_3 and IF_1 may give rise to a distinct response to microwave radiation. For instance, the resonance response at $\nu = 1.3$ exhibits strong dependence on B-field orientation: although weak resonance features are detectable with an out-of-plane B field, there is no resonance signal in the presence of an in-plane B field (Fig. 2a). Given the distinct behaviour, the mechanism underlying the extremely weak signal at $\nu = +1.2$ probably differs from $\nu = \pm 2.0$. As the latter is the main focus of this work, we will leave further investigations of the former response for future efforts.

Next, we examine the microwave-induced resonance features in the density range of moiré filling $2 < |\nu| < 3$ and identify its relationship with the isospin order associated with the Dirac revivals at $|\nu| = 2$ (refs. 2,3). Figure 3a shows the locations of r_1 that are extracted from the waterfall plot in Fig. 1g and marked with red circles. The observed linear trajectory exhibits a slope that corresponds to an electron g-factor of 2. This is a strong indication that the transport response originates from an electron spin resonance. Interestingly, the linear trajectory of r_1 extrapolates to a negative intercept with the frequency axis at $B = 0$, which provides the finger print to identify the nature of this collective excitation. Given the phase space defined by spin, valley isospin and sublattice, it is recognized that the Dirac revival at half-filling could give rise to 15 possible order parameters[32]. Out of these options, the linear slope of $g = 2$ is most naturally explained by two candidate orders—a state with parallel (ferromagnetic) spin polarization in the two valleys and an antiferromagnetic state where the spins are anti-aligned (the 'Magnon spectra and microwave resonance' section in the Supplementary Information provides a more detailed discussion). The nature of the valley-dependent spin configuration is determined by the intervalley Hund's interaction J_H, with $J_H < 0$ (expected for Coulomb interactions[18]) and $J_H > 0$ corresponding to parallel and anti-parallel spins, respectively.

In the presence of a ferromagnetic Hund's coupling ($J_H < 0$), there will be a single Goldstone mode for vanishing magnetic field $\vec{B} = 0$, as a consequence of the spontaneously broken spin-rotation symmetry. Although gapless at $\vec{B} = 0$, this mode will exhibit a finite gap $\Delta = g\mu_B|\vec{B}|$ when $\vec{B} \neq 0$, determined by the spin Zeeman energy. Here μ_B denotes the Bohr magneton. The resonance behaviour of this Goldstone mode is shown in Fig. 3b (red solid line). In the case of $J_H < 0$, the $|\vec{B}|$ dependence of all the microwave resonance frequencies is linear and those associated with single-magnon processes have a slope $g\mu_B/h$. The intercept will be zero for the resonance with the lowest energy, which appears at the lowest microwave frequency. This behaviour is not consistent with the experiment where the lowest and most dominant resonance mode exhibits a negative intercept.

Let us, therefore, consider the case $J_H > 0$, where the spins in opposite valleys are anti-parallel at $\vec{B} = 0$ (Fig. 3c, inset). When we turn on

https://doi.org/10.1038/s41567-023-02060-0

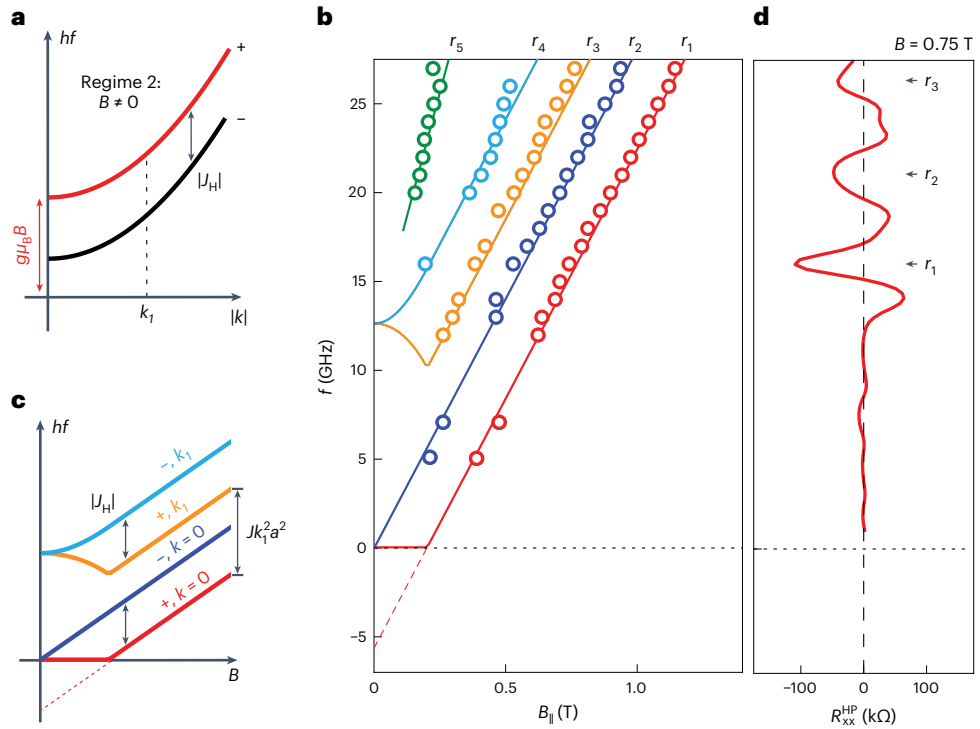

Fig. 4 | Spin stiffness and dispersion. a, Schematic of the magnon dispersion in regime 2, characterized by field B as well as J_H. **b**, Locations of r_1–r_5, marked with red, blue, orange, cyan and green circles, respectively, in the f–B data. The solid lines correspond to the theoretical fit for the resonance modes. **c**, Schematic of the magnon spectrum resulting from an antiferromagnetic intervalley coupling. The red and blue lines correspond to the $k = 0$ modes, whereas the orange and cyan lines denote geometric resonance modes with $k \neq 0$. The offset between the $k = 0$ and k_1 modes is characterized by $Jk_1^2a^2$, where J is a measure of spin stiffness and a is the moiré lattice constant. **d**, Vertical linecut from the f–B resonances at $B = 0.75$ T, where the minima in R_{xx}^{HP} are the locations of the first three modes r_1–r_3.

the external magnetic field ($\vec{B} \neq 0$), anti-parallel spins are canted with their ferromagnetic (antiferromagnetic) components along (perpendicular to) $\vec{B}$ (Fig. 3d, regime 1). When $g\mu_B|\vec{B}| \geq J_H$ (regime 2), the antiferromagnetic component vanishes and the spins are fully aligned with the magnetic field. In the antiferromagnetic case, the resonance behaviour of the lowest-energy excitation is shown in Fig. 3c (red solid line). It remains gapless for $\vec{B} \neq 0$ in regime 1, which derives from breaking the single continuous symmetry given by spin rotations along the magnetic-field axis[33]. In regime 2, however, it develops a non-zero gap given by $\Delta = g\mu_B|\vec{B}| - J_H$, which extrapolates to $B = 0$ with a negative intercept of $\Delta f = -J_H/h$. This is in excellent agreement with the observed behaviour of r_1, providing a strong indication for $J_H > 0$. Most remarkably, the measured intercept from mode r_1, which corresponds to the Goldstone mode (−) in regime 1, allows us to extract the value of J_H. A negative intercept of $\Delta f = -5.6$ GHz (Fig. 3b) yields an intervalley Hund's coupling of $J_H = 0.023$ meV, which is compatible with numerical estimates of $J_H = 0.075$ meV (ref. 18).

The correlation-driven origin of r_1 is further supported by the lack of a resonance response in other graphene monolayer and bilayer samples, including TBG with a large twist angle where the influence of correlation is minimized by the highly dispersive energy band structure. In these samples, flatband physics such as Dirac revival is absent and the underlying Fermi surface is IU, making them directly comparable with the IU regime of magic-angle TBG. All these graphene samples feature doubly encapsulated geometry with hexagonal boron nitride and graphite encapsulation to minimize the influence of charge fluctuation and outside impurities on the resonance measurement (the 'ESR measurement in graphene monolayer and bilayer samples: the absence of resonance response' section in the Supplementary Information provides more details on sample characterization). Despite the excellent sample quality, spin resonance measurements on these graphene monolayer and bilayer samples, using the same setup shown in Fig. 1a, show no indication of any microwave-induced resonance signal over a large range of microwave frequency, power and charge carrier density across both electron- and hole-type carrier polarities (Supplementary Figs. 7–10, 12 and 13). These observations offer further confirmation that the strong resonance response in TBG is intrinsic to the flat moiré energy band and directly associated with the isospin order underlying the Dirac revival at $\nu = \pm 2$. The lack of a resonance response in high-quality graphene monolayer and bilayer samples is in stark contrast with previous spin resonance experiments[34–36] on unencapsulated monolayer graphene samples prepared with the chemical vapour deposition method, which have known material issues[34,35]. It has been well documented in the literature that transport response across graphene is highly susceptible to the influence of outside disorder and impurity. As such, encapsulation with hexagonal boron nitride and graphite is essential in probing the intrinsic behaviours of graphene[37–41].

Taken together, our understanding of the origin of r_1, which is associated with the intervalley exchange interaction J_H in the IF_2 regime, is supported by a number of prominent experimental characteristics: (1) r_1 is the fundamental resonance mode that is detectable at the lowest microwave power; (2) the resonance behaviour of r_1 tracks a linear trajectory in the f–B map that extrapolates to a negative intercept at $B = 0$; (3) the behaviour of r_1 remains the same with in-plane and out-of-plane magnetic fields; (4) prominent resonance response is observed only in the density regime that corresponds to an isospin ferromagnet with twofold degeneracy (IF_2), whereas no resonance is observed in the IU regime; (5) using the same experimental setup, we observe no indication of a resonance response in graphene monolayer and bilayer samples without a flat moiré band.

Having established a theoretical model for understanding the r_1 mode, we are now in a position to investigate higher-order resonance

modes r_2–r_5. Here r_2 can be understood by simply considering the valley degrees of freedom. The spin configuration of the resonance mode can be either in phase across the two valleys or out of phase. For simplicity, we will refer to the in-phase and out-of-phase modes as $p = +$ and $-$, respectively. Given the antiferromagnetic coupling across two valleys, $p = -$ is favoured as the lowest-energy mode. The energy gap of mode +, on the other hand, is given by the Zeeman energy. As a result, mode + corresponds to a straight line with slope $g\mu_B/h$ and a vanishing intercept (Fig. 3c, blue solid line), which is consistent with the trajectory displayed by the r_2 mode. Compared with r_1, r_2 requires a higher microwave power to be detectable (Supplementary Fig. 1). This is consistent with the overall hierarchy among all the resonance signals.

The magnon picture and geometric resonances of r_1 and r_2 also capture the behaviours of r_3 and r_4. This can be understood by considering the energy spectrum of the magnon modes (Fig. 4a and Supplementary Fig. 14). In regime 2, the spectrum varies quadratically at small $\vec{k}$, that is, $\Delta E_{\vec{k}} \approx J\vec{k}^2 a^2$, where a is the moiré lattice constant and J provides a measure of the spin stiffness (the 'Dirac revival from spin polarization and resonance frequencies' section in the Supplementary Information provides a more detailed definition of J). Both r_1 and r_2 correspond to the zero-momentum ($\vec{k} = 0$) limit of this magnon spectrum. The finite size of the sample induces standing magnon waves, which correspond to spin resonance with non-zero momentum. In the simplest picture, the geometric resonance could occur as $\vec{k}$ takes a set of discrete values, which are given by $\vec{k} = 2\pi(n/L_x, m/L_y)^T$, where $n, m \in \mathbb{Z}$. Here $L_x \times L_y$ defines the rectangular dimensions of the sample.

The geometric resonance with the lowest energy occurs at momentum k_1 defined by $(n, m) = (1, 0)$ or $(0, 1)$. This gives rise to two extra resonance modes in the f–B map, namely, $+, k_1$ and $-, k_1$. In particular, $+, k_1$ is expected to exhibit an offset relative to $-, k_1$ that is given by $|J_H|$. This is in excellent agreement with the observed behaviour of r_3 and r_4 (Fig. 4b), which are offset by the same amount as r_1 ($+, k = 0$) and r_2 ($-, k = 0$), respectively.

Although the simple model of magnon geometric resonance provides an excellent explanation for the observed resonances of r_3 and r_4, our Hall-bar-shaped sample is not the ideal geometry for detecting geometric resonance, as it lacks a well-defined boundary that could form a cavity. The lack of clear boundaries makes it impossible to quantitatively extract spin stiffness J from the data. Although we cannot rigorously exclude that some of r_2–r_4 may have an origin distinct from r_1, the lack of magnetic anisotropy in the resonance response provides a strong indication that the influence of spin–orbit coupling is negligible. As shown in Fig. 2a and Supplementary Fig. 3, the dispersion of all the resonance modes in the f–B data remains the same for in-plane and out-of-plane B fields. The lack of magnetic anisotropy suggests that the strength of the spin–orbit coupling is much smaller than 100 μeV, which is consistent with the upper bound value of 40 μeV extracted from the coercive field of the orbital ferromagnetism[12]. Within the experimental uncertainty, which results from the width of the resonance mode and is roughly the size of the circles shown in Fig. 4b, the r_5 mode has a slope of $g = 4$ in the f–B map. Following the same model for r_1–r_4, r_5 can be naturally understood by considering a two-magnon mode[42,43].

In summary, our findings imply an antiferromagnetic alignment of the spins in opposite values in the doping range of $2 \le |\nu| \le 3$ and provide the first experimental determination of the sign and value of the intervalley Hund's interaction $J_H = 0.023$ meV. This is a crucial parameter, which also determines the spin structure of the superconducting order parameter: for the antiferromagnetic sign that we extract, the order parameter is expected to be either a spin-singlet state or a singlet–triplet admixed state[19]; the latter admixed state must be realized, if superconductivity coexists microscopically with the isospin order that we identified. We note that this conclusion is consistent with a recent analysis[44] of the body of other experiments on TBG and twisted trilayer graphene. Moreover, the ability of our microwave study to probe J_H could shed light onto the mechanism underlying the intervalley exchange interaction. It has been proposed that a Coulomb interaction leads to a ferromagnetic coupling and a negative J_H, whereas the contribution from the electron–phonon interaction favours an antiferromagnetic coupling and a positive J_H (ref. 18). Although our results appear to indicate that the electron–phonon coupling plays a more dominant role, combining microwave measurements with Coulomb screening in future experiments would allow us to untangle the role of Coulomb interaction and electron–phonon coupling in determining J_H. Finally, our microwave resonance probe of collective modes would also enable us to identify exotic emergent symmetries in other twisted graphene superlattices[45].

Online content

Any methods, additional references, Nature Portfolio reporting summaries, source data, extended data, supplementary information, acknowledgements, peer review information; details of author contributions and competing interests; and statements of data and code availability are available at https://doi.org/10.1038/s41567-023-02060-0.

References

1. Park, J. M., Cao, Y., Watanabe, K., Taniguchi, T. & Jarillo-Herrero, P. Flavour Hund's coupling, Chern gaps and charge diffusivity in moiré graphene. *Nature* **592**, 43–48 (2021).
2. Zondiner, U. et al. Cascade of phase transitions and Dirac revivals in magic-angle graphene. *Nature* **582**, 203–208 (2020).
3. Wong, D. et al. Cascade of electronic transitions in magic-angle twisted bilayer graphene. *Nature* **582**, 198–202 (2020).
4. Lu, X. et al. Superconductors, orbital magnets, and correlated states in magic angle bilayer graphene. *Nature* **574**, 653–657 (2019).
5. Cao, Y. et al. Correlated insulator behaviour at half-filling in magic-angle graphene superlattices. *Nature* **556**, 80–84 (2018).
6. Yankowitz, M. et al. Tuning superconductivity in twisted bilayer graphene. *Science* **363**, 1059–1064 (2019).
7. Cao, Y. et al. Unconventional superconductivity in magic-angle graphene superlattices. *Nature* **556**, 43–50 (2018).
8. Sharpe, A. L. et al. Emergent ferromagnetism near three-quarters filling in twisted bilayer graphene. *Science* **365**, 605–608 (2019).
9. Serlin, M. et al. Intrinsic quantized anomalous Hall effect in a moiré heterostructure. *Science* **367**, 900–903 (2020).
10. Chen, S. et al. Electrically tunable correlated and topological states in twisted monolayer–bilayer graphene. *Nat. Phys.* **17**, 374–380 (2021).
11. Polshyn, H. et al. Electrical switching of magnetic order in an orbital Chern insulator. *Nature* **588**, 66–70 (2020).
12. Lin, J.-X. et al. Spin-orbit–driven ferromagnetism at half moiré filling in magic-angle twisted bilayer graphene. *Science* **375**, 437–441 (2022).
13. Chen, G. et al. Tunable correlated Chern insulator and ferromagnetism in a moiré superlattice. *Nature* **579**, 56–61 (2020).
14. Xu, C. & Balents, L. Topological superconductivity in twisted multilayer graphene. *Phys. Rev. Lett.* **121**, 087001 (2018).
15. Isobe, H., Yuan, N. F. Q. & Fu, L. Unconventional superconductivity and density waves in twisted bilayer graphene. *Phys. Rev. X* **8**, 041041 (2018).
16. You, Y.-Z. & Vishwanath, A. Superconductivity from valley fluctuations and approximate SO(4) symmetry in a weak coupling theory of twisted bilayer graphene. *npj Quantum Mater.* **4**, 16 (2019).
17. Zhang, Y.-H., Mao, D., Cao, Y., Jarillo-Herrero, P. & Senthil, T. Nearly flat Chern bands in moiré superlattices. *Phys. Rev. B* **99**, 075127 (2019).
18. Chatterjee, S., Bultinck, N. & Zaletel, M. P. Symmetry breaking and skyrmionic transport in twisted bilayer graphene. *Phys. Rev. B* **101**, 165141 (2020).

19. Scheurer, M. S. & Samajdar, R. Pairing in graphene-based moiré superlattices. *Phys. Rev. Res.* **2**, 033062 (2020).
20. Kang, J., Bernevig, B. A. & Vafek, O. Cascades between light and heavy fermions in the normal state of magic-angle twisted bilayer graphene. *Phys. Rev. Lett.* **127**, 266402 (2021).
21. Khalaf, E., Bultinck, N., Vishwanath, A. & Zaletel, M. P. Soft modes in magic angle twisted bilayer graphene. Preprint at https://arxiv.org/abs/2009.14827 (2020).
22. Bernevig, B. A. et al. Twisted bilayer graphene. V. Exact analytic many-body excitations in Coulomb Hamiltonians: charge gap, Goldstone modes, and absence of Cooper pairing. *Phys. Rev. B* **103**, 205415 (2021).
23. Christos, M., Sachdev, S. & Scheurer, M. S. Correlated insulators, semimetals, and superconductivity in twisted trilayer graphene. *Phys. Rev. X* **12**, 021018 (2022).
24. Huang, C., Wei, N., Qin, W. & MacDonald, A. H. Pseudospin paramagnons and the superconducting dome in magic angle twisted bilayer graphene. *Phys. Rev. Lett.* **129**, 187001 (2022).
25. Kumar, A., Xie, M. & MacDonald, A. H. Lattice collective modes from a continuum model of magic-angle twisted bilayer graphene. *Phys. Rev. B* **104**, 035119 (2021).
26. Schrade, C. & Fu, L. Spin-valley density wave in moiré materials. *Phys. Rev. B* **100**, 035413 (2019).
27. Saito, Y. et al. Isospin Pomeranchuk effect in twisted bilayer graphene. *Nature* **592**, 220–224 (2021).
28. Rozen, A. et al. Entropic evidence for a Pomeranchuk effect in magic-angle graphene. *Nature* **592**, 214–219 (2021).
29. Liu, X., Zhang, N., Watanabe, K., Taniguchi, T. & Li, J. Isospin order in superconducting magic-angle twisted trilayer graphene. *Nat. Phys.* **18**, 522–527 (2022).
30. Liu, X. et al. Tuning electron correlation in magic-angle twisted bilayer graphene using Coulomb screening. *Science* **371**, 1261–1265 (2021).
31. Sharpe, A. L. et al. Evidence of orbital ferromagnetism in twisted bilayer graphene aligned to hexagonal boron nitride. *Nano Lett.* **21**, 4299–4304 (2021).
32. Christos, M., Sachdev, S. & Scheurer, M. S. Superconductivity, correlated insulators, and Wess–Zumino–Witten terms in twisted bilayer graphene. *Proc. Natl Acad. Sci. USA* **117**, 29543–29554 (2020).
33. Watanabe, H. Counting rules of Nambu–Goldstone modes. *Annu. Rev. Condens. Matter Phys.* **11**, 169–187 (2020).
34. Mani, R. G., Hankinson, J., Berger, C. & De Heer, W. A. Observation of resistively detected hole spin resonance and zero-field pseudo-spin splitting in epitaxial graphene. *Nat. Commun.* **3**, 996 (2012).
35. Sichau, J. et al. Resonance microwave measurements of an intrinsic spin-orbit coupling gap in graphene: a possible indication of a topological state. *Phys. Rev. Lett.* **122**, 046403 (2019).
36. Singh, U. R. et al. Sublattice symmetry breaking and ultralow energy excitations in graphene-on-hBN heterostructures. *Phys. Rev. B* **102**, 245134 (2020).
37. Wang, L. et al. One-dimensional electrical contact to a two-dimensional material. *Science* **342**, 614–617 (2013).
38. Zibrov, A. A. et al. Tunable interacting composite fermion phases in a half-filled bilayer-graphene Landau level. *Nature* **549**, 360–364 (2017).
39. Li, J. I. A. et al. Even-denominator fractional quantum Hall states in bilayer graphene. *Science* **358**, 648–652 (2017).
40. Zeng, Y. et al. High-quality magnetotransport in graphene using the edge-free Corbino geometry. *Phys. Rev. Lett.* **122**, 137701 (2019).
41. Polshyn, H. et al. Quantitative transport measurements of fractional quantum Hall energy gaps in edgeless graphene devices. *Phys. Rev. Lett.* **121**, 226801 (2018).
42. Chinn, S. R., Zeiger, H. J. & O'Connor, J. R. Two-magnon Raman scattering and exchange interactions in antiferromagnetic $KNiF_3$ and K_2NiF_4 and ferrimagnetic $RbNiF_3$. *Phys. Rev. B* **3**, 1709–1735 (1971).
43. Davies, R. W. Amplitude-renormalization factor in two-magnon Raman scattering. *Phys. Rev. B* **5**, 4598–4602 (1972).
44. Lake, E., Patri, A. S. & Senthil, T. Pairing symmetry of twisted bilayer graphene: a phenomenological synthesis. *Phys. Rev. B* **106**, 104506 (2022).
45. Wilhelm, P., Lang, T. C., Scheurer, M. S. & Läuchli, A. M. Non-coplanar magnetism, topological density wave order and emergent symmetry at half-integer filling of moiré Chern bands. *SciPost Phys.* **14**, 040 (2023).

Methods

Standard methods for device fabrication and quantum transport measurement are detailed in the Supplementary Information. For the microwave measurements shown in the main text, longitudinal resistance R_{xx} is measured when sweeping the external magnetic field, either in the in-plane or out-of-plane orientation. In the case of the f–B data, a B-field sweep is performed with a fixed microwave frequency, that is, B is the fast axis and the microwave frequency is the slow axis. Along the same vein, B is again the fast axis and moiré filling ν is the slow axis for the ν–B maps. In this case, microwave power and frequency are fixed at constant values for the entire measurement. To eliminate the slow-varying B-dependent background in R_{xx}, an HPF is added in the post-measurement analysis for each B-sweep line. The cutoff frequency of the HPF, which is in arbitrary units that only depends on the density of B points, is chosen in a way that it does not interfere with the microwave-induced resonance features.

Data availability

Source data are available for this paper. All other data that support the findings of this study are available from the corresponding authors upon reasonable request.

Acknowledgements

A.M and J.I.A.L. thank R. Cong for the critical review of the manuscript. E.M. acknowledges funding from the National Defense Science and Engineering Graduate (NDSEG) Fellowship. J.-X.L. and J.I.A.L. acknowledge funding from NSF DMR-2143384. The device fabrication was performed at the Institute for Molecular and Nanoscale Innovation at Brown University. J.P. and L.Z. acknowledge support from the Cowen Family Endowment at MSU. K.W. and T.T. acknowledge support from the EMEXT Element Strategy Initiative to Form Core Research Center by grant no. JPMXP0112101001 and the CREST(JPMJCR15F3), JST. Sandia National Laboratories is a multi-mission laboratory managed and operated by the National Technology and Engineering Solutions of Sandia, LLC, a wholly owned subsidiary of Honeywell International, Inc., for the US Department of Energy (DOE)'s National Nuclear Security Administration under contract DE-NA0003525. This work was funded, in part, by the Laboratory Directed Research and Development Program and performed, in part, at the Center for Integrated Nanotechnologies, an Office of Science User Facility operated for the US DOE, Office of Science. This paper describes the objective technical results and analysis. Any subjective views or opinions that might be expressed in the paper do not necessarily represent the views of the US DOE or the US government.

Author contributions

J.-X.L. and E.M. fabricated the device. E.M, A.M., D.S., L.Z. and J.P. performed the measurements. E.M., A.M. and J.I.A.L. analysed the data. E.M., M.S.S., A.M. and J.I.A.L. wrote the manuscript. S.L., D.R. and J.H. provided the WSe_2 crystals. K.W. and T.T. provided the hexagonal boron nitride crystals.

Competing interests

A provisional patent application has been filed in the USA. by Brown University under serial no. 18/103,290. The inventors include J.I.A.L., A.M., E.M. and J.-X.L. The application, which is pending, contains proposals of two-dimensional material architectures with controllable magnetic states and microwave resonance.

Additional information

Supplementary information The online version contains supplementary material available at https://doi.org/10.1038/s41567-023-02060-0.

Correspondence and requests for materials should be addressed to Andrew Mounce or J. I. A. Li.

Peer review information *Nature Physics* thanks the anonymous reviewers for their contribution to the peer review of this work.